ACS Biomaterials SCIENCE & ENGINEERING

pubs.acs.org/journal/abseba

Article

Three-Dimensional Lymphatics-on-a-Chip Reveals Distinct, Size-Dependent Nanoparticle Transport Mechanisms in Lymphatic Drug Delivery

Renhao Lu, Benjamin J. Lee, and Esak Lee*

Cite This: https://doi.org/10.1021/acsbiomaterials.4c01005

Read Online

ACCESS | Metrics & More | Article Recommendations | Supporting Information

ABSTRACT: Although nanoparticle-based lymphatic drug delivery systems promise better treatment of cancer, infectious disease, and immune disease, their clinical translations are limited by low delivery efficiencies and unclear transport mechanisms. Here, we employed a three-dimensional (3D) lymphatics-on-a-chip featuring an engineered lymphatic vessel (LV) capable of draining interstitial fluids including nanoparticles. We tested lymphatic drainage of different sizes (30, 50, and 70 nm) of PLGA-*b*-PEG nanoparticles (NPs) using the lymphatics-on-a-chip device. In this study, we discovered that smaller NPs (30 and 50 nm) transported faster than larger NPs (70 nm) through the interstitial space, as expected, but the smaller NPs were captured by lymphatic endothelial cells (LECs) and accumulated within their cytosol, delaying NP transport into the lymphatic lumen, which was not observed in larger NPs. To examine the mechanisms of size-dependent NP transports, we employed four inhibitors, dynasore, nystatin, amiloride, and adrenomedullin, to selectively block dynamin-, caveolin-, macropinocytosis-mediated endocytosis-, and cell junction-mediated paracellular transport. Inhibiting dynamin using dynasore enhanced the transport of smaller NPs (30 and 50 nm) into the lymphatic lumen, minimizing cytosolic accumulation, but showed no effect on larger NP transport. Interestingly, the inhibition of caveolin by nystatin decreased the lymphatic transport of larger NPs without affecting the smaller NP transport, indicating distinct endocytosis mechanisms used by different sizes of NPs. Macropinocytosis inhibition by amiloride did not change the drainage of all sizes of NPs; however, paracellular transport inhibition by adrenomedullin blocked the lymphatic transport of NPs of all sizes. We further revealed that smaller NPs were captured in the Rab7-positive late-stage lymphatic endosomes to delay their lymphatic drainage, which was reversed by dynamin inhibition, suggesting that Rab7 is a potential target to enhance the lymphatic delivery of smaller NPs. Together, our 3D lymphatics-on-a-chip model unveils size-dependent NP transport mechanisms in lymphatic drug delivery.

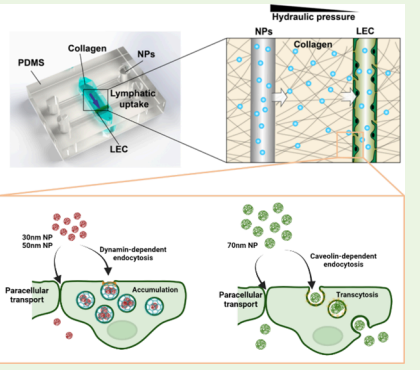

KEYWORDS: *nanoparticle, lymphatics, microfluidics, drug delivery, paracellular, intracellular, dynamin, caveolin, endocytosis*

INTRODUCTION

The lymphatic system comprises the lymphatic vessel network and lymphoid organs.[1] Lymphatic vessels (LVs) drain excess interstitial fluid to form a lymph and then transport the lymph to bigger LVs and lymph nodes (LNs) and ultimately to the blood circulation through the subclavian veins.[2−5] The LVs provide routes for antigens, antigen-presenting cells (APCs), and lymphocytes to traffic to draining LNs and regulate adaptive immune responses. In addition, LVs are major routes for lymph node tumor metastasis in many types of cancers.[6,7] Since lymphatics play a role in the immune system and cancer, there have been interests in lymphatic drug delivery to treat those diseases.[8−13]

Nanoparticles (NPs) have been used as drug and vaccine carriers to deliver them to LNs through peripheral LVs.[14] Upon subcutaneous injection, while water-soluble small molecules primarily diffuse into blood capillaries with tight junctions, NPs with an average 10−100 nm hydrodynamic size preclude ready access to the blood system due to their larger size. Instead, NPs drain into LVs through the unique and permeable cell−cell junctions and discontinuous basement membranes in the lymphatic endothelium.[15,16] Engineered NPs containing various drugs, antigens, or mRNAs have been developed to deliver them to the lymphatic system.[11,17,18] Swartz et al. developed polypropylene sulfide NPs with the sizes of 25 and 100 nm, and observed 25 nm NPs can efficiently reach the draining LNs, target the resident dendritic cells, and activate immune response.[16] They also developed 30 nm adjuvanted NPs to target tumor-draining LNs and reshape T cell immunity.[19] Thomas et al. incorporated degradable

Received: May 30, 2024
Revised: August 16, 2024
Accepted: August 20, 2024

linkers with their lymphatic-targeting NPs to boost the immune response.[20] Bay K8644 NPs were developed by Thomas et al. to target collecting LVs and improve lymphatic functions.[9] Porter et al. developed methods to target lymphatics via oral delivery of lipophilic prodrugs.[21]

Despite substantial progress in lymphatic drug delivery, relatively fewer nanomedicines on the market achieve desirable pharmacokinetics or therapeutic efficacies through lymphatic delivery.[22] This is partially due to the unclear delivery mechanisms and biodistribution of NPs through the lymphatic system.[23] A few studies have examined lymphatic transport, measuring their delivery efficiencies, which varied depending on models (5−40% of the dose).[24] Studies have suggested that the NP size would be one of the factors in determining lymphatic delivery rates: 20 and 40 nm NPs had 15.4 and 15.8% delivery rates to the draining LNs 24 h after subcutaneous injection, respectively, which were higher than the delivery rate with 100 nm NPs.[17] However, most of the injected NPs are still retained in the injection sites, needing further improvement.

Utilizing in vitro bioengineered models as a test platform to screen NPs can be a smart approach. Several models have been developed to study NP transport kinetics, including multicellular spheroids,[25] hydrogels,[26] and three-dimensional (3D) bioprinted tissues.[27] These platforms allowed in situ, real-time, high-resolution biomedical monitoring of NP trafficking, which has often been difficult in settings of in vivo animal models.[28] Meanwhile, transwell has also been used to study NP transport across two-dimensional (2D) endothelial cell layers.[29−31] Microfluidic organ-on-a-chip platforms can integrate an extracellular matrix (ECM), multiple cell types, and 3D lymphatic structures, which can better reconstruct the tissue microenvironment. By our group and others, such models have shown promising results in blood and lymphatic vasculature modeling and cellular interactions[4,32−35] but have not yet been used for studying lymphatic NP delivery.

In this study, we utilized a previously developed microfluidic lymphatics-on-a-chip that integrates ECM and an engineered lymphatic vessel (LV) that drains interstitial fluids.[36] We included nanoparticles (NPs) in the interstitial fluids to model the physiological environment near the subcutaneous injection site and study the NP drainage into LVs. We tested PLGA-*b*-PEG NPs with different sizes (30, 50, and 70 nm) in our lymphatics-on-a-chip device and investigated size-dependent NP transport mechanisms in lymphatic drug delivery. Here, we discovered that smaller NPs (30 and 50 nm) that moved faster than larger NPs (70 nm) in the interstitium were surprisingly captured by LVs and accumulated within the cytosol of lymphatic endothelial cells (LECs), delaying their transport to the lymphatic lumen, which was not observed in the larger NPs. Our investigation with four different inhibitors to block dynamin-, caveolin-, and macropinocytosis-dependent endocytosis and the paracellular transport revealed that inhibiting dynamin-dependent endocytosis enhanced the transport of smaller NPs (30 and 50 nm) into the lymphatic lumen by minimizing cytosolic accumulation but showed no effect on the transport of larger NPs (70 nm). By contrast, the inhibition of caveolin decreased the lymphatic transport of larger NPs without affecting the transport of the smaller NPs, indicating distinct endocytosis mechanisms that are used by NPs of different sizes. Finally, we unveiled that smaller NPs accumulated in the Rab7-positive late-stage lymphatic endosomes, delaying their entry into the lymphatic lumen, which was reversed by dynamin blockade, suggesting Rab7 as a potential target to enhance the lymphatic delivery of smaller NPs.

MATERIALS AND METHODS

Nanoparticles. Poly(lactic-*co*-glycolic)-*b*-poly(ethylene glycol) nanoparticles (NPs) conjugated with Cy7.5 carboxylic acid and Alexa488 carboxylic acid dyes with number-average diameters of 30, 50, and 70 nm were prepared and characterized by Dr. Hai-Quan Mao (Johns Hopkins University).[17] NPs were lyophilized and shipped. Upon receiving, each nanoparticle formulation was reconstituted to 1 mg/mL with 10% w/v sucrose and further diluted to 100 μg/mL NPs in PBS for measuring its nanoparticle hydrodynamic diameter (number-average) and zeta potential with a Malvern Zetasizer Nano ZS.

Cell Culture. Three different cell strains of human dermal lymphatic endothelial cells (LECs), isolated from dermal tissues of neonatal donors, were kindly donated by Dr. Young Kwon Hong (University of Southern California). These cells have been characterized using several lymphatic endothelial markers in Dr. Hong's lab.[37,38] LECs were cultured in EGM-2MV media (Lonza, Switzerland), used until their passage 7, and maintained in standard tissue culture incubators at 37 °C, 95% humidity, and 5% CO_2.

Microfluidic Device Fabrication. As we performed previously, microfluidic devices were fabricated using a soft lithography method.[36,39,40] A molded wafer was microfabricated with SU-8 photoresist and coated with a monolayer of tridecafluoro-1,1,2,2-tetrahydrooctyl trichlorosilane (FOTS). The polydimethylsiloxane (PDMS, Sylgard 184, Dow-Corning, Midland, MI) was mixed with a curing agent from the Sylgard PDMS kit at a 10:1 ratio of base to curing agent and poured onto the model wafer for overnight curing at 80 °C. After removal from the molds, the PDMS was trimmed, and reservoir and collagen entries were made with 6 and 2 mm biopsy punches (Integra, Princeton, NJ, USA), respectively. The device was assembled by bonding the PDMS gasket on top of a glass coverslip with plasma etching and overnight incubation at 80 °C. Afterward, the devices were plasma-treated, coated with 0.01% poly-L-lysine (Sigma, St Louis, MO) for 1 h and 1% glutaraldehyde for 30 min with three times washing in between, and then rinsed thoroughly overnight. Then, bovine serum albumin (BSA)-coated, sterilized 250 μm steel acupuncture needles were introduced into the device channels. Rat tail collagen 1 hydrogel (Corning, at final collagen concentration: 2.5 mg/mL) was pipetted into the devices and cross-linked at 37 °C overnight. The next day, the acupuncture needles were removed and the openings for needle insertion were blocked with vacuum grease. The channels were washed overnight on the rocker with a full medium before cell seeding. To seed lymphatic endothelial cells (LECs) to the channel, enzymatically dislodged (0.05% trypsin/EDTA, Gibco, New York, NY, USA) LECs were resuspended at 2×10^6 cells/mL in full media, and 100 μL of cell suspension was introduced into the right-side channel of the device via the medium reservoirs that are connected to the right-side hollow channel, allowing cells to adhere to the collagen matrix for 10 min upside down and right-side up before washing with growth medium. The devices were incubated on a rocking platform in a humidified tissue culture incubator (5% CO_2, 37 °C), replenishing culture media daily.

Volume Drainage and NP Lymphatic Delivery Measurement. For measuring lymphatic volume drainage and NP lymphatic delivery in the lymphatics-on-a-chip device, fresh reconstituted NPs with different sizes were diluted with the EGM-2MV medium solution at 0.1 mg/mL and added to the reservoirs on the acellular channel side to establish an interstitial fluid pressure gradient across the collagen hydrogel toward the engineered LV. An NP suspension (150 μL) was added to each reservoir on the acellular channel side, and 10 μL of the full medium was added to each reservoir on the lymphatic channel side. For inhibitor treatments, lymphatics-on-a-chip devices were preincubated with adrenomedullin (100 nM, Sigma, #A2327), dynasore (80 μM, Sigma, #SIAL-D7693), nystatin (80 μM, Sigma, #1477003), and amiloride (80 μM, Sigma, #A7410) to block

https://doi.org/10.1021/acsbiomaterials.4c01005
ACS Biomater. Sci. Eng. XXXX, XXX, XXX−XXX

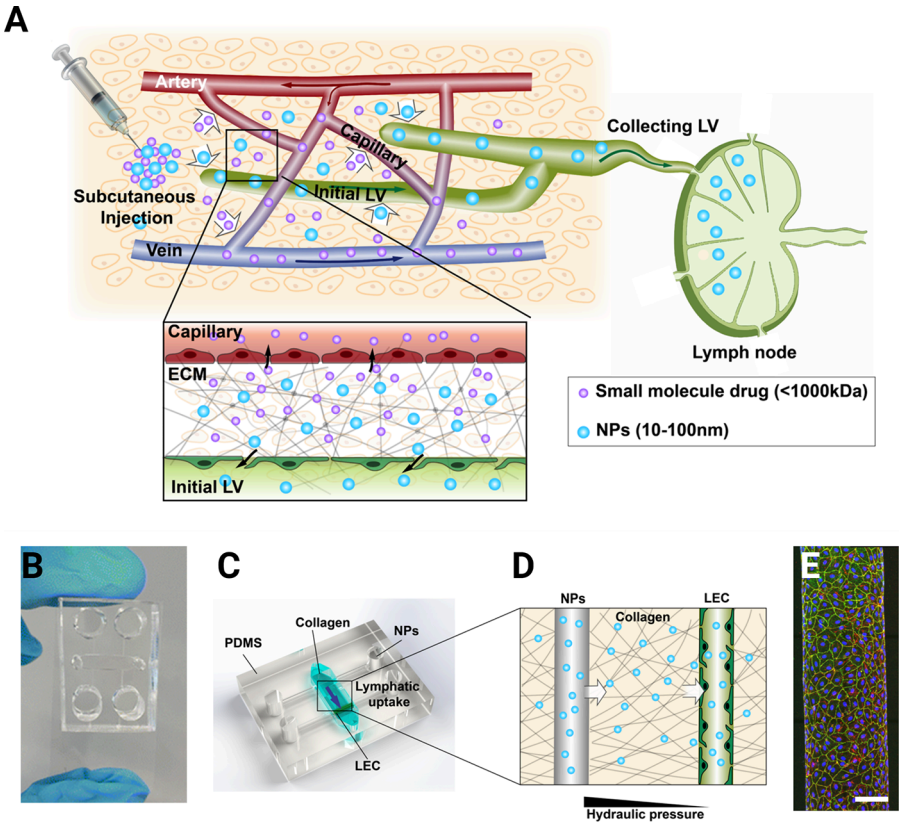

Figure 1. 3D lymphatics-on-a-chip model to decipher size-dependent nanoparticle (NP) transport into lymphatic vessels (LVs). (A) Schematic of the NP drug delivery system. Upon subcutaneous injection, water-soluble molecules (<1000 kDa) are collected by the blood capillary; however, NPs (10−100 nm) are preferably drained into the lymphatic vessels via their permeable junctions and reach draining lymph nodes. (B, C) Picture and schematic of the lymphatics-on-a-chip model. The collagen bulk (blue) represents the 3D interstitial space, with ECM proteins penetrated by two hollow channels. (D) One of the channels seeded with lymphatic endothelial cells (LECs) forms an engineered LV. The second, cell-free channel allows the introduction of excess fluid to form an interstitial fluid pressure gradient between the acellular and lymphatic channels. Simulating subcutaneous NP injection, excess media, including NPs, are loaded into the acellular channel. NPs transport through the interstitial ECM space, reach the engineered LV, and drain into the LV. Drained and remaining NPs are collected from the 4 circular reservoirs for analysis. (E) Representative image of an engineered LV stained with anti-VE-cadherin (adherens junction, green) antibodies, phalloidin (F-actin, red), and DAPI (nucleus, blue). Scale bar in (E): 100 μm.

paracellular transport and dynamin-, caveolin-, and macropinocytosis-dependent endocytosis. DMSO vehicles were used as controls. After 2 h of inhibitor/DMSO treatment, NP lymphatic drainage experiments were performed by adding the excess volume of NP suspension, including the same dose of inhibitors or DMSO, to the acellular channel to trigger interstitial flow to the LV channel. After 12 h of drainage, the media in both the acellular and lymphatic channel sides were collected, with their volumes V_1 and V_2, respectively, determined by weight, and the percentage volume drainage was calculated using eq 1 as follows:

$$\text{volume drainage } \% = V_2 \div (V_1 + V_2) \times 100\% \quad (1)$$

Volume drainage (abluminal to luminal) was measured to assess the boundary function of the lymphatic vessel. Due to the function of the primary lymphatic valve,[41] the permeability test measuring the opposite transport (luminal to abluminal transport) can be significantly different from the abluminal-to-luminal drainage;[39,42,43] hence, the permeability was not tested in this study. In our other studies, the average permeability of lymphatic endothelium with a perfusable lumen was 2.5×10^{-5} cm/s with 70 kDa dextran (from a previous study).[32]

Next, the concentration of NPs was measured by a fluorescent signal using a SpectraMax M2Microplate Reader (Molecular Devices, San Jose, CA) and SoftMax Pro 7 software with a standard curve of known concentrations in media. The NP standard curve was generated in full medium with DMSO or inhibitors with the same treatment concentration and used to obtain the mass of NPs based on the volume in the collected samples. NP delivery efficiency was calculated by dividing the NP amount in the lymphatic channel side by the total NP amount.

Immunostaining. Due to the NP signal decay following permeabilization, NP and other proteins were imaged separately and then aligned afterward. The lymphatics-on-a-chip devices were first fixed with 4% paraformaldehyde (Electron Microscopy Sciences, Hatfield, PA) and stained with DAPI (Sigma, 1:500), and images of nucleic acids and NPs (FITC) were captured. Then, devices were permeated with PBST (0.3% Triton-X in PBS) and blocked with 3% BSA in PBS overnight at 4 °C. Primary antibodies detecting Rab7 (Cell Signaling, 1:100, #95746) were incubated in a blocking buffer overnight at 4 °C and then washed with PBS three times. Secondary antibodies (all from Invitrogen, Waltham, MA, 1:500) were subsequently incubated in a blocking buffer overnight at 4 °C in the dark and washed with PBS three times. After capturing images of DAPI and Rab7, NP and Rab7 images were aligned with the reference of DAPI. Confocal images were acquired with an SP8 confocal microscope (Leica) with 10× and 40× objectives. Obtained fluorescence images were z-stacked and adjusted for brightness and contrast using ImageJ.[44] Image alignment was performed with the MultiStackReg plugin[45] in ImageJ, and Pearson's colocalization coefficient analysis was performed with the JACoP plugin[46] in ImageJ.

Statistics. Independent two-sample populations were compared using an unpaired, two-tailed Student's t test with a normal distribution assumption. For group analyses, one-way ANOVAs

https://doi.org/10.1021/acsbiomaterials.4c01005
ACS Biomater. Sci. Eng. XXXX, XXX, XXX−XXX

with Tukey's HSD (honestly significant difference) tests were used to compare the mean values. All p values were two-sided, and $*p < 0.05$ was considered statistically significant. All information regarding the number of experimental repeats and sample sizes was included in figure legends, where the N number indicates biological replicates, such as individual microfluidic devices or well within well plates. Statistical analyses were performed using Microsoft Excel. All data points on the graphs represent average values, and error bars depict the standard error of the mean (SEM).

RESULTS

3D Lymphatics-on-a-Chip Model to Examine NP Transport to Lymphatics. To reconstitute NP delivery to peripheral lymphatic vessels (LVs) (Figure 1A), we employed a 3D microfluidic lymphatics-on-a-chip model developed previously (Figure 1B).[36] The device comprises two microchannels fully embedded in the central ECM chamber (2.5 mg/mL collagen I with ~4.4 μm average pore size) (Figure 1C).[47] Rat tail collagen I was used, given that it has been extensively tested with human endothelial cells, and collagen I is highly conserved across species.[48] One of the microchannels was seeded with three different cell strains of human dermal lymphatic endothelial cells (LECs from three neonatal donors) to model the engineered lymphatic vessel (LV) (Figure 1D). The counterpart microchannel was acellular (cell-free) and filled with NP suspension to introduce excess interstitial fluid, which generates an interstitial fluid pressure gradient between the two channels. The NPs suspended in the interstitial fluid convected through ECM, reached the LV, and drained into the LV. We collected the drained fluid for NP transport analysis (Figure 1D). By locating the device on a rocker during the drainage experiment, we also generated a luminal shear flow of approximately 3.5−4.5 dyn/cm^2 to maintain healthy engineered LV. As shown in Figure 1E, the engineered LV formed a nice monolayer of lymphatic endothelium with VE-cadherin-positive adherens junctions and an average permeability of 2.5 × 10^{-5} cm/s with 70 kDa dextran (from our previous study[32]). Taken together, we created a 3D lymphatics-on-a-chip to model NP transport into lymphatics.

Nanoparticle (NP) Characterization. PLGA-*b*-PEG NPs with different sizes (30, 50, and 70 nm) were characterized to confirm their size distribution, uniformity, and surface charges after interlab transportation. Dynamic light scattering confirmed the diameter of each nanoparticle batch and showed a semibroad distribution of sizes (Figure 2A,B). The resulting polydispersity index (PDI) for each nanoparticle was between 0.15 and 0.25, confirming that the NPs for each diameter were mostly homogeneous (Figure 2C). The zeta potential of each NPs was negative, with all sizes of NPs having similar surface charges (Figure 2D). To confirm the NP stability, we further incubated NPs in PBS and EBM-2 (serum-free cell culture medium) for 12 h at 37 °C and compared their size distribution and zeta potential. As shown in Supplementary Figure 1, the size distribution of all NPs remained stable, with a slight decrease in surface charge (but with no significant differences before and after incubations). Taken together, PLGA-*b*-PEG NPs were stable enough and kept similar sizes and surface charges after the interlab transportation, storage, and incubation in media for 12 h, which is within the time frame as our lymphatic drainage experiments are performed overnight and is a much shorter time frame regarding PLGA NP degradation, typically requiring several days to weeks.[49,50]

Smaller NPs Transport Faster than Larger NPs through the 3D Collagen ECM. Using the lymphatics-on-a-chip device, we first tested the delivery efficiency of NPs with different sizes (30, 50, and 70 nm) in the collagen I ECM without any lymphatic endothelial barrier in the right-sided channel (both channels were acellular) (Figure 3A). As shown in Figure 3B, NPs with all three sizes exhibited a relatively high delivery ratio (>40%), and 30 nm NPs showed a significantly higher delivery ratio than 70 nm NPs, which aligns with previous studies.[16,17] Such fast NP transport is mainly due to the large porous structure of collagen gel with ~4.4 μm average pore size.[47] Meanwhile, NPs of different sizes did not change the fluid drainage dynamics in the ECM according to the volume drainage measurement (Figure 3C), indicating that the size-dependent NP delivery in the ECM is not due to the altered interstitial flow profile but mainly due to different NP sizes. A time course measurement of the volume drainage and the 50 nm NP delivery showed that the fluid flow decreased over time due to the reduction of the hydraulic pressure difference between the two channels (Figure 3D). The NP delivery was lower than the volume drainage and remained steady within 8 h. Faster volume drainage may increase the NP concentration in the acellular channel, accelerate diffusion according to Fick's Law, and compensate for decreased interstitial fluid flow.[51] Taken together, smaller NPs transport faster through 3D collagen than larger NPs, providing the baseline for later analyzing the NP transports with lymphatic vessels.

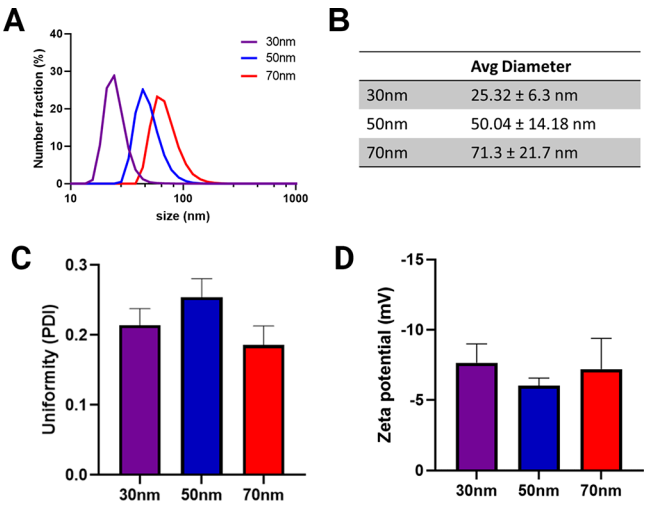

Figure 2. Nanoparticle (NP) characterization. (A) Dynamic light scattering measurements of NP size distributions. (B) Quantitative measurements of average NP diameters with a margin of error. (C) Polydispersity index (PDI) of the NPs. (D) Zeta potential of the NPs.

Engineered LVs Capture Smaller NPs and Delay NP Drainage into the Lymphatic Lumen. Next, we examined the contribution of the lymphatic barrier in NP transport in the system by comparing the NP delivery efficiencies in acellular vs lymphatics-on-a-chip devices (Figure 4A). NP delivery efficiency was measured by examining the volume of drained fluid and the FITC fluorescence signal of the PLGA-*b*-PEG NPs in the drained fluid. Our model could decouple the NP transport resistance from ECM and lymphatics by comparing the NP delivery in acellular devices with that in lymphatics-on-a-chip devices, which can be difficult to investigate using conventional in vivo models. Although smaller NPs transported faster than larger NPs through the ECM in acellular environments (Figure 3B), the results in the lymphatics-on-a-

https://doi.org/10.1021/acsbiomaterials.4c01005
ACS Biomater. Sci. Eng. XXXX, XXX, XXX−XXX

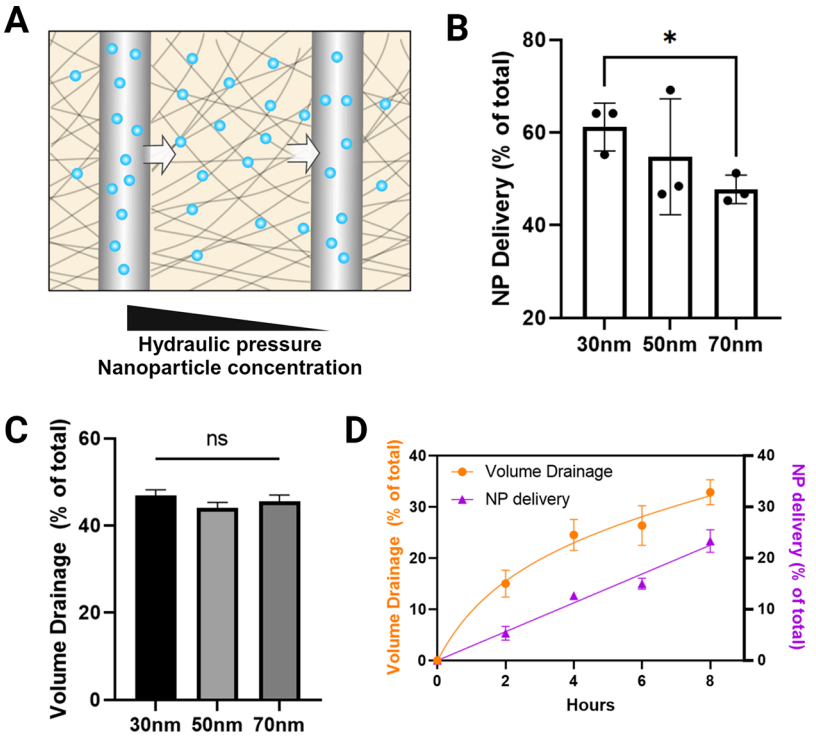

Figure 3. Smaller NPs transport faster through 3D collagen ECM than larger NPs. (A) Schematic of the acellular experimental setup. NPs loaded in the left-side channel are transported through the porous ECM and collected in reservoirs connected to the right-side channel. (B) Delivery ratio of NPs with different sizes in collagen ECM ($N = 3$). (C) Volume drainage in the collagen ECM when different-sized NPs are loaded ($N = 3$). (D) Time course measurement of volume drainage and 50 nm NP delivery in 8 h ($N = 3$). *$p < 0.05$ indicates statistical significance. "ns" indicates no significance.

chip were surprising (Figure 4B). Smaller NPs (30 and 50 nm) showed significantly lower delivery efficiency in the presence of LECs than in acellular conditions. However, larger NPs (70 nm) showed no differences with or without LECs in the system (Figure 4B). We further evaluated the NP resistance contributed by LVs by calculating the ratio of lymphatic and acellular devices' delivery efficiencies. LVs showed almost no resistance to 70 nm NPs (~90% ratio) but significantly resisted the transport of smaller NPs (30 and 50 nm) (50−60% ratio, Figure 4C). We hypothesized that the NPs are trapped within cell layers to show much resistance and performed fluorescence microscopy (Figure 4D). Fluorescence microscopy showed the accumulation of 30 and 50 nm NPs within the cytosol of lymphatic endothelial cells (LECs). In contrast, 70 nm NPs were distributed almost randomly across the LECs (Figure 4D). The 3D-rendered and cross-sectional views with 50 nm NPs in Figure 4E,F further confirmed the smaller NP distribution inside the LECs of the engineered LVs. Taken together, engineered LVs delay the drainage of smaller NPs by capturing them within the cytosol of LECs but do not affect the drainage of the larger NPs (70 nm).

Testing Out Dynasore, Nystatin, Amiloride, and Adrenomedullin Reveals Size-Dependent Mechanisms in NP Transport through the Lymphatic Endothelium. Next, we sought to understand size-dependent mechanisms of NP transport through the lymphatic endothelium, addressing how smaller NPs were accumulated in the LEC cytosol (but not larger NPs) and how the cytosolic accumulation is regulated. To examine the mechanisms of size-dependent NP transport, we employed four different transport inhibitors: dynasore, nystatin, amiloride, and adrenomedullin (Figure 5A). We treated our lymphatics-on-a-chip device with dynasore (80 μM) to inhibit dynamin-mediated endocytosis, nystatin (80 μM) to block caveolin-dependent endocytosis, amiloride (80 μM) to inhibit macropinocytosis-mediated endocytosis, and adrenomedullin (100 nM) to block cell junction-mediated paracellular transport (Figure 5A). Dynamin inhibition with dynasore significantly increased the transport of smaller NPs (30 and 50 nm) into the lymphatic lumen (increased NP delivery) but did not alter the transport of the 70 nm NPs (Figure 5B). By contrast, the inhibition of caveolin by nystatin decreased the lymphatic transport of larger NPs without affecting the transport of smaller NPs (Figure 5C). These data indicate that NPs of different sizes use distinct endocytosis mechanisms when they traffic through the lymphatic endothelium. Smaller NPs (30 nm, 50 nm) are endocytosed via dynamin-mediated mechanisms, resulting in cytosolic accumulation of NPs and the delay of NP transport out of the cells into the lymphatic lumen, which is reversed by dynasore treatment; thus, dynasore treatment promotes lymphatic delivery of smaller NPs. By contrast, larger NPs (70 nm) are endocytosed through caveolin-dependent mechanisms, leading to continued transcytosis with no cytosolic accumulation, which can facilitate NP delivery to lymphatic lumens and can be blocked by nystatin treatment; thus, nystatin treatment slows down lymphatic delivery of larger NPs (Figure 5B,C). Next, amiloride was treated to block macropinocytosis-mediated endocytosis. Amiloride treatment did not affect the delivery of NPs of all sizes (Figure 5D), suggesting that macropinocytosis may not be the major pathway for NP transport through lymphatics. Last, adrenomedullin treatment to block the cell junction-mediated paracellular transport decreased the delivery of all-sized NPs (Figure 5E), demonstrating the significance of the junction-

https://doi.org/10.1021/acsbiomaterials.4c01005
ACS Biomater. Sci. Eng. XXXX, XXX, XXX−XXX

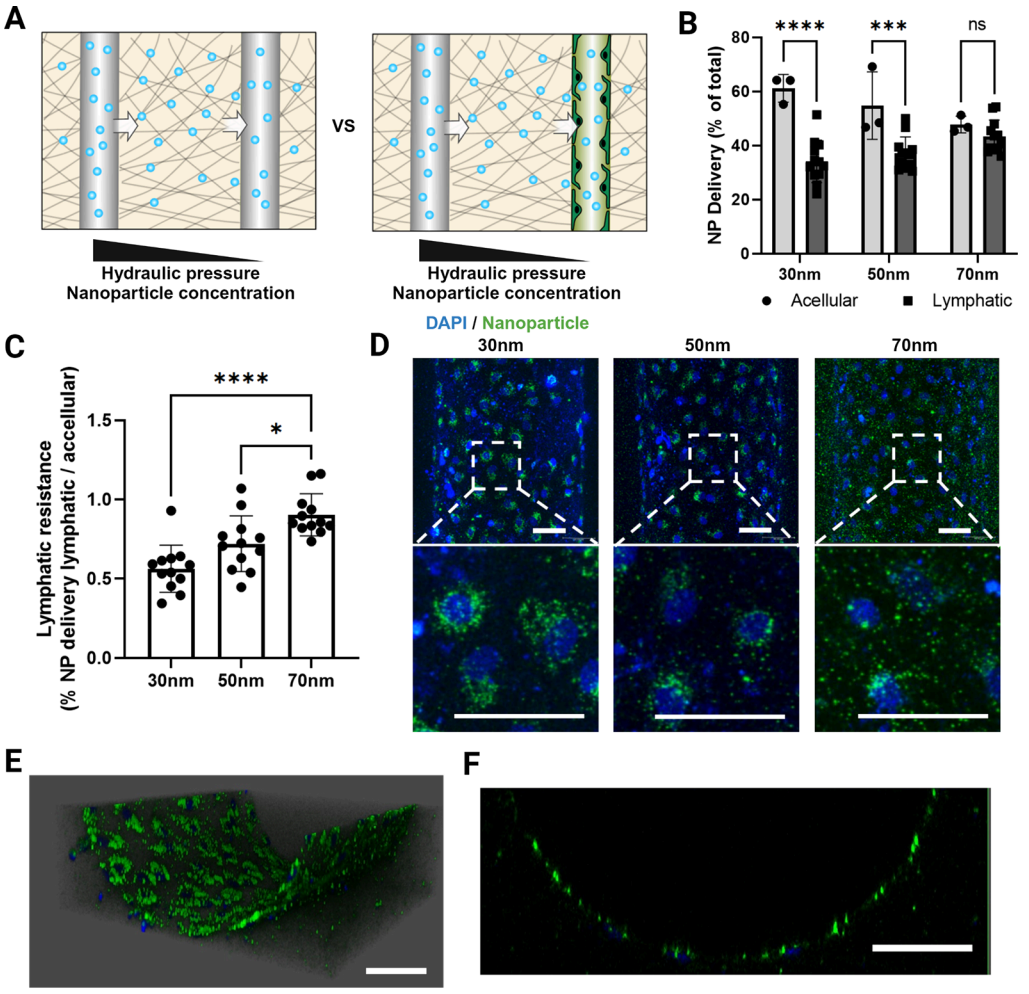

Figure 4. Engineered LVs capture smaller NPs and delay NP drainage into the lymphatic lumen, which is not shown with larger NPs. (A) Experimental schematic of NP drainage with or without LECs. (B) Percent NP delivery of different sizes of NPs in acellular vs lymphatic chips (N = 3−12). (C) Percent lymphatic resistance (ratio of NP delivery in lymphatic and acellular chips) (N = 3−12). (D) Confocal images of NP localization with an engineered LV. (E, F) 3D-rendered and cross-sectioned LV images with 50 nm NP trafficking. Scale bars in panels (D)−(F): 50 μm. *p < 0.05, ***p < 0.001, and ****p < 0.0001 indicate statistical significance. "ns" indicates no significance.

mediated paracellular transport in NP transport through the lymphatic endothelium in addition to the various endocytosis pathways described above. In all cases, volume drainage was similar (Figure 5F), which indicates that the different NP transport results were due to NP−cellular interactions, not by any altered interstitial flow profile. Taken together, all-sized NPs utilize junction-mediated paracellular transport; however, smaller NPs, in particular, use dynamin-dependent endocytosis, which can hinder NP export to lymphatic lumens by accumulating NPs within the cells (Figure 5G). Contrastingly, larger NPs rely on caveolin-dependent endocytosis and transcytosis to facilitate NP transport to lymphatic lumens (Figure 5H). All of the readouts with testing dynasore, nystatin, amiloride, and adrenomedullin revealed size-dependent NP transport mechanisms through lymphatics, which are summarized in Figure 5I.

Smaller NPs Accumulate in the Rab7-Positive Late-Stage Lymphatic Endosomes, Which Is Reversed by Dynamin Blockade. To understand where the smaller NPs accumulate in LECs via dynamin-dependent mechanisms (Figure 6A), we stained the late-stage endosome marker Rab7 (red) after finishing the NP (green) delivery experiments (Figure 6B). In merged images of red and green colors, yellow indicates red (Rab7) and green (NPs) colocalization, showing more cellular accumulation NPs in the late-stage endosomes. In smaller NPs (30 and 50 nm), DMSO-treated control conditions showed the higher colocalization of NPs (green) and Rab7 (red), whereas dynasore treatment led to less colocalization of NPs and Rab7 (Figure 6B). Rab7 colocalization with different sizes of NPs was quantified by obtaining Pearson's colocalization coefficients (Figure 6C). Higher Pearson's coefficients in the DMSO-treated group being tested with smaller NPs indicate the accumulation of NPs within Rab7-positive endosomes in LECs. Meanwhile, dynasore significantly decreased the colocalization of Rab7 with the NPs. These trends were not observed when there were larger (70 nm) NPs. Taken together, smaller NPs accumulate in the Rab7-positive late-stage lymphatic endosomes, which is reversed by dynamin blockade, suggesting Rab7 as a potential target to enhance the lymphatic delivery of smaller NPs.

DISCUSSION

In this study, we utilized a microfluidic organ-on-a-chip device to model the nanoparticle (NP) delivery to the lymphatics in vitro, where PLGA-*b*-PEG NPs with different sizes pass

https://doi.org/10.1021/acsbiomaterials.4c01005
ACS Biomater. Sci. Eng. XXXX, XXX, XXX−XXX

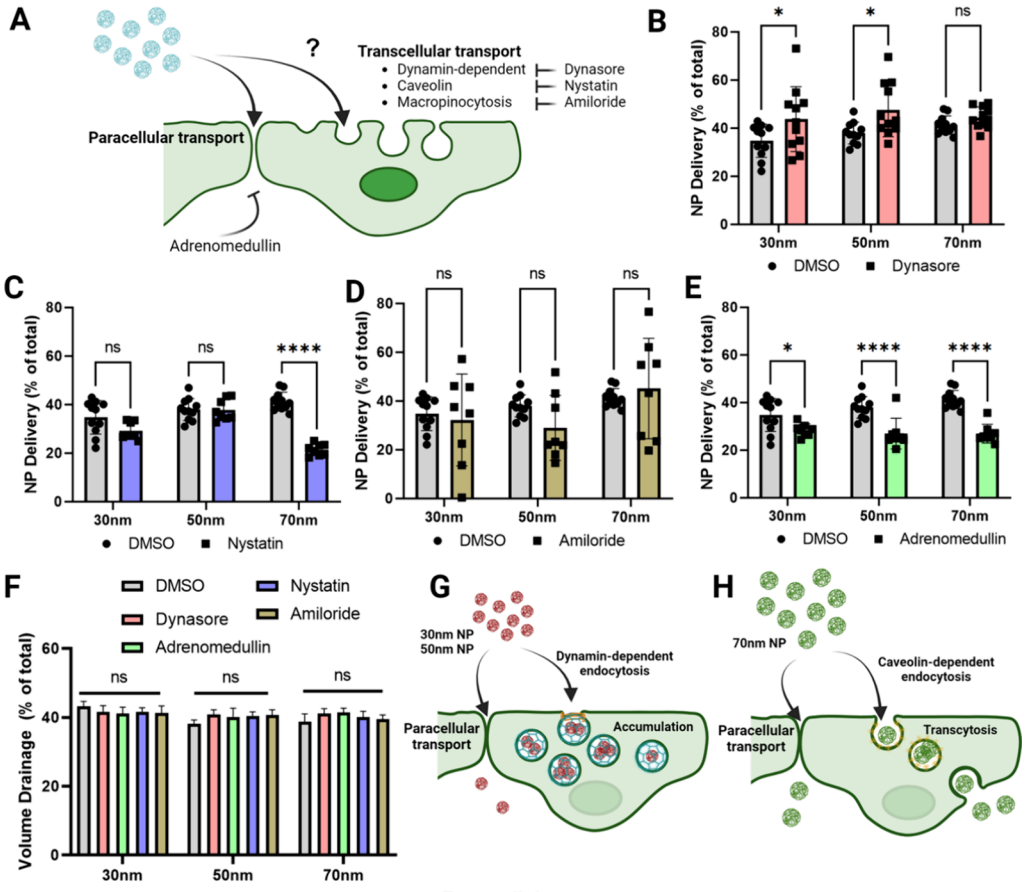

I

		Paracellular	Transcellular: Dynamin	Transcellular: Caveolin	Transcellular: Macropinocytosis	Accumulation	Delivery
30nm	DMSO	High	High	—	—	High	Low
	Dynasore	High	Low	—	—	Low	High
	Nystatin	High	High	—	—	High	Low
	Amiloride	High	High	—	—	High	Low
	Adrenomedullin	Low	High	—	—	High	Low
50nm	DMSO	High	High	—	—	High	Low
	Dynasore	High	Low	—	—	Low	High
	Nystatin	High	High	—	—	High	Low
	Amiloride	High	High	—	—	High	Low
	Adrenomedullin	Low	High	—	—	High	Low
70nm	DMSO	High	Low	High	—	Low	High
	Dynasore	High	Low	High	—	Low	High
	Nystatin	High	Low	Low	—	Low	Low
	Amiloride	High	Low	High	—	Low	High
	Adrenomedullin	Low	Low	High	—	Low	Low

Figure 5. Testing out dynasore, nystatin, amiloride, and adrenomedullin reveals size-dependent mechanisms of NP transport through lymphatics. (A) Schematic of NP transport pathways and their inhibitors. (B−E) NP delivery with 80 μM dynasore (B), 80 μM nystatin (C), 80 μM amiloride (D), and 100 nM adrenomedullin (E) treatments (N = 8−11). (F) Volume drainage with NPs of different sizes with or without different endocytosis inhibitors (N = 8−11). (G) Schematic of smaller NP (30 and 50 nm) transports through lymphatics. (H) Schematic of larger NP (70 nm) transports through the lymphatics. (I) Summary of the size-dependent NP transport mechanisms through the lymphatic endothelium. *p < 0.05, and ****p < 0.0001 indicate statistical significance. "ns" indicates no significance.

through an interstitial space of collagen gel first and then drain into the engineered LV. In the interstitial space, smaller NPs (30 and 50 nm) moved faster than larger NPs (70 nm). However, the smaller NPs were retained inside LECs at the lymphatic boundary and showed a delivery rate that was lower than that of larger NPs (70 nm). By various transport inhibitor treatments, we revealed that paracellular transport contributes to all-sized NP delivery. Surprisingly, caveolin-dependent endocytosis positively contributes to larger NP (70 nm) delivery, and dynamin-dependent endocytosis negatively

https://doi.org/10.1021/acsbiomaterials.4c01005
ACS Biomater. Sci. Eng. XXXX, XXX, XXX−XXX

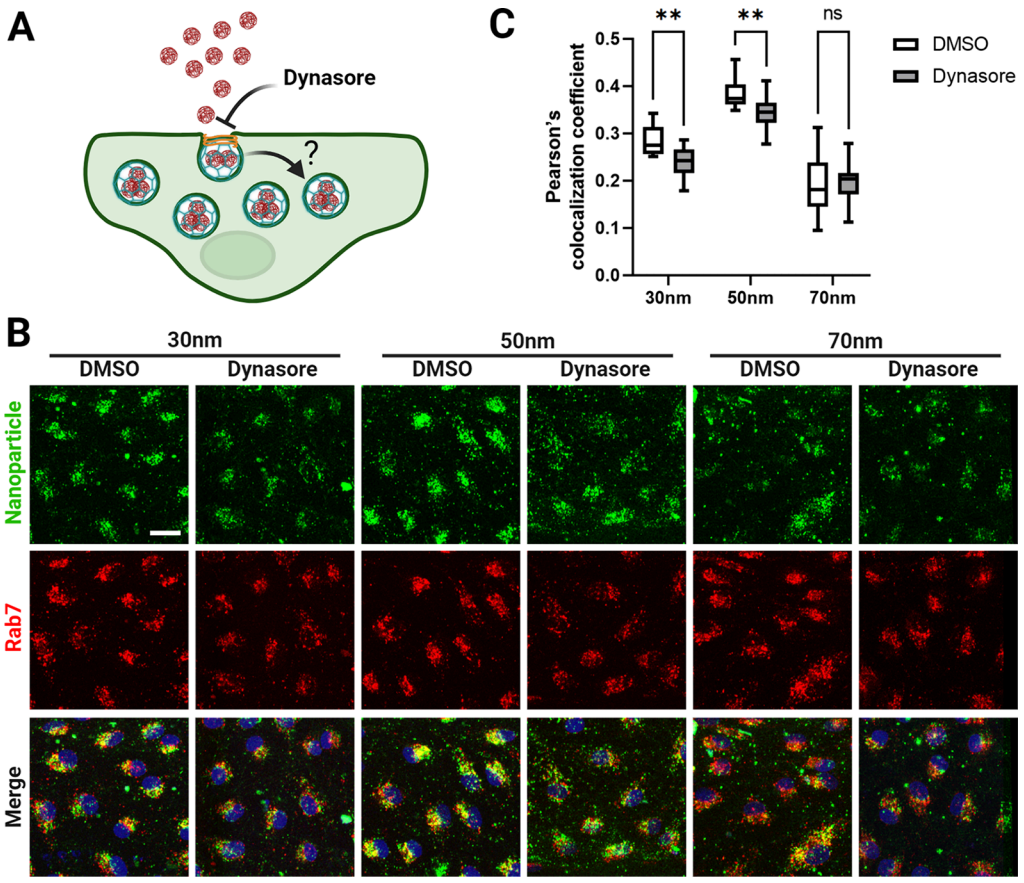

Figure 6. Smaller NPs accumulate in the Rab7-positive late-stage lymphatic endosomes, which is reversed by dynamin blockade. (A) Schematic of smaller NP transports through lymphatics, which can be captured by dynamin-dependent cytosolic accumulation. (B) Fluorescence images of Rab7 (red)-stained LECs with NPs (green) show NP colocalization with the late endosome marker Rab7. (C) Quantification of NP and Rab7 colocalization with Pearson's colocalization coefficients ($N = 8$). Scale bar: (B) 25 μm. **$p < 0.01$ indicates statistical significance. "ns" indicates no significance.

contributes to smaller NP (30 and 50 nm) delivery (Figure 5). We further showed that the retention of smaller NPs was due to dynamin-dependent endocytosis and cytosolic accumulation within Rab7-positive late-stage endosomes, which was blocked by dynasore treatment to increase the rate of export of smaller NPs out of cells and transport to the lymphatic lumen (Figure 6).

Previous studies have shown NP transport across LVs via paracellular and transcellular mechanisms.[14,52] The initial LVs have sparse basement membranes and oak leaf-shaped LECs with "button-like" cell junctions formed by discontinuous adherens and tight junction protein complexes.[53] Such a structure is believed to facilitate paracellular NP transport. Meanwhile, transcellular transport is also important for fluid and macromolecular transport, including hyaluronic acid, chylomicron, lipoproteins, albumin-bound fatty acids, etc.[24,54] During transcellular transport across LECs, NPs are first taken up into cell surface caveolae (endocytosis), transported across the cell, and released (exocytosis) on the other side.[55] The major types of endocytosis include clathrin-coated pit-mediated endocytosis (CME), fast endophilin-mediated endocytosis (FEME), caveolin-dependent endocytosis, clathrin-independent carrier (CLIC) endocytosis, macropinocytosis, and phagocytosis.[56] Among them, CME and FEME are dynamin-dependent. In our studies, although both dynamin and caveolin contribute to NP delivery, the transported NP sizes were different and the overall delivery outcomes were opposite (Figure 5). The colocalization of NPs with the late endosome marker Rab7[57] suggests the fate of NPs within lysosomes but not exocytosis. Furthermore, dynasore treatment decreased the colocalization and increased the delivery of 30 and 50 nm NPs, implying that dynamin-dependent endosomes preferably accumulated intracellularly. On the other hand, 70 nm NP delivery can be increased by caveolin but did not show significant colocalization with Rab7, potentially indicating that 70 nm NPs were transported through caveosomes.[58] How caveolin-dependent endocytosis causes transcytosis but dynamin-dependent mechanisms do not in the lymphatic endothelium with differently sized NPs remains to be investigated further.

The size of NPs has been a critical factor for lymphatic uptake from the interstitial space,[59] and previous studies have identified ~25 nm as an optimal size for lymphatic delivery. For example, 25 nm polypropylene sulfide NPs showed significantly higher LN delivery efficiency compared with 100 nm NPs according to Swartz's group.[16] Another study from Thomas' group showed that 25 nm dextran had higher LN delivery compared with 10, 12, and 54 nm dextran.[60] But at the same time, controversial in vivo observations exist. Some others' previous in vivo studies indicate that lymphatics may preferentially uptake NPs in the 50−100 nm range.[29,61] Another in vivo study also reveals that 50−100 nm NP has significantly extended lymph node retention compared with 15 nm NP, suggesting the advantage of larger nanoparticles for

https://doi.org/10.1021/acsbiomaterials.4c01005
ACS Biomater. Sci. Eng. XXXX, XXX, XXX−XXX

vaccine delivery.[62] We believe that these discrepancies arise from differences in the contribution of transport resistance among models, including both in vitro and in vivo models. The ECM and lymphatic vessel (LV) wall are two major barriers to NP delivery, but the relative contributions of these barriers can be variable among experiment setups. Both in vivo and in vitro studies, including our results, have shown that smaller NPs migrate much faster through the ECM.[24] However, when it comes to the LV wall as a main barrier, our system contributes to the community with a new discovery that different endocytosis mechanisms can be used by LECs when they meet NPs of different sizes. Especially when smaller NPs are used, they can be captured within LECs, delaying their actual entry into the lymphatic lumen and system, which can be prevented by dynamin or Rab7 inhibitions. However, larger NPs use caveolin, which does not accumulate NPs within cytosol, with less worry about delays. These mechanisms are required for further investigation in vivo to determine whether these mechanisms can synergize lymphatic delivery.

Considering that the in vivo ECM has a highly complex and dense structure with smaller pores, whereas the collagen hydrogel in our in vitro model has relatively large pores and offers less resistance to NPs of all sizes, the ECM resistance may be more significant in vivo, while lymphatic resistance may be more significant in vitro. Tissue ECM is highly selective in filtering the local transport of macromolecules and constitutes an important barrier toward infectious agents.[63] Tumor-targeting NPs are usually restricted near the perivascular region and trapped in the tumor ECM instead of diffusing successfully into the deep tumor areas.[64] Lymphatic-targeting NPs exhibit retention near the injection site regardless of their size,[17] suggesting that ECM is one of the major barriers to NP delivery. Although the size-dependent NP transport in ECM has been studied in silico,[65] in vitro,[63,66,67] and in vivo,[17] NP transport mechanisms through the ECM are more complicated due to the inherent mesh-like organization[67] and are not completely understood. In this study, we observed that NP transport is driven by a combination of convection and diffusion, and smaller NP transport is faster in collagen ECM than larger NPs. However, the collagen ECM in our model is simplified, lacking other ECM components, including proteoglycans, glycosaminoglycans, hyaluronan, etc.[68] The pore size of type I collagen hydrogel (~4.4 μm[48]) is larger than that of dermal tissue (~0.79 μm[69]); hence, NPs with all sizes showed a relatively higher delivery ratio within our acellular devices than a previous in vivo study.[17] Better models with more in vivo-like ECM using decellularized ECM components would better model the system to recapitulate both ECM and LV wall barriers more appropriately.

NP nonspecific delivery and accumulation in off-target sites can decrease delivery efficiency and lead to unexpected cytotoxicity.[70] NP biodistribution within the endothelium, another major barrier to NP delivery, remains unclear.[71] Previous studies have shown NP accumulation in the blood–brain barrier (BBB) in vitro and in silico due to fast endocytosis and slow exocytosis.[72,73] Still, the NP distribution in normal blood vessels or LVs has not been reported yet. In this study, for the first time, we reported that NP can also accumulate in LEC in a size-dependent manner, potentially serving as a hurdle in lymphatic drug delivery. But at the same time, this would be a great opportunity if we want to deliver some things directly to LECs for other purposes. Future lymphatic-targeting NP strategies may need to consider the potential accumulation and cytotoxicity in LECs depending on the size and other physiochemical properties of NPs. Meanwhile, such properties of NP accumulation in LECs can also be utilized to deliver drugs specifically to LVs instead of draining LNs. Recently, Sestito et al. (in Thomas and Dixon's groups) developed a 30 nm NP with Bay K8644 payload to increase lymphatic pumping and observed the presence of NP in collecting LV endothelium,[9] which aligns with our findings. Such an approach can increase the drug delivery efficiency and reduce the drug exposure to other tissues. Also, endocytosis inhibition has been shown to increase paracellular transport[29] and has been utilized as an NP delivery strategy to avoid off-target accumulation and degradation.[74,75]

As we discussed, there are several limitations in our current model system that need further improvement. First, besides paracellular and transcellular transport, NPs can also be taken up by dendritic cells and subsequently migrate into the lymphatic system.[24] Integrating dendritic cells and other third-type cell components into our model would allow us to better investigate these indirect transport pathways in the NP transport. Second, our current model only includes LECs in monolayers, whereas NPs need to transit through collecting LVs covered by lymphatic muscle cells and lymphatic valves regulate unidirectional lymph flow to reach LNs. A recent study has shown that NPs can accumulate in collecting LVs after entering the lymphatic vessels,[9] suggesting potential NP trafficking directly to collecting LVs. Incorporating these elements would provide a more comprehensive understanding of NP transport within the lymphatic system. Also, as we discussed in earlier paragraphs, our current ECM model contains only type I collagen with a pore size larger than that found in dermal tissues. Including additional ECM components and achieving a more physiologically relevant pore structure would greatly enhance the model's accuracy. Last, the study was not supported by in vivo validations, which guarantees further investigation of animal models.

CONCLUSIONS

In this study, we employed a microfluidic lymphatics-on-a-chip model featuring an engineered lymphatic vessel (LV) draining interstitial fluid with differently sized nanoparticles (NPs). Contrary to existing beliefs that NPs ranging from 10 to 100 nm efficiently migrate into the lymphatics, our study suggests that NPs of different sizes use distinct transport pathways, which can impact the transport of NPs into the lymphatic lumen. Smaller NPs (30 and 50 nm) are endocytosed via dynamin-mediated mechanisms, leading to intracellular accumulation and delayed transport out of cells into the lymphatic lumen, a process that can be reversed by dynasore treatment, thereby promoting lymphatic delivery. In contrast, larger NPs (70 nm) are endocytosed through caveolin-dependent mechanisms, facilitating transcytosis without cytosolic accumulation, which enhances delivery to the lymphatic lumen but can be inhibited by nystatin treatment, thus slowing their lymphatic delivery. In summary, our 3D lymphatics-on-a-chip model unveils size-dependent NP transport mechanisms in lymphatic drug delivery and provides a platform to screen lymphatic drug delivery systems.

ASSOCIATED CONTENT

Data Availability Statement

All source data are available in the main text or the Supporting Information. The corresponding authors can provide addi-

https://doi.org/10.1021/acsbiomaterials.4c01005
ACS Biomater. Sci. Eng. XXXX, XXX, XXX−XXX

tional data supporting this study's findings upon reasonable request.

Supporting Information

The Supporting Information is available free of charge at https://pubs.acs.org/doi/10.1021/acsbiomaterials.4c01005.

Supplementary Figure 1: nanoparticle (NP) degradation characterization over 12 h (PDF)

AUTHOR INFORMATION

Corresponding Author

Esak Lee − *Nancy E. and Peter C. Meinig School of Biomedical Engineering, Cornell University, Ithaca, New York 14853, United States;* orcid.org/0000-0002-5328-6677; Phone: 607-255-8491; Email: el767@cornell.edu

Authors

Renhao Lu − *Nancy E. and Peter C. Meinig School of Biomedical Engineering, Cornell University, Ithaca, New York 14853, United States*

Benjamin J. Lee − *Nancy E. and Peter C. Meinig School of Biomedical Engineering, Cornell University, Ithaca, New York 14853, United States*

Complete contact information is available at: https://pubs.acs.org/10.1021/acsbiomaterials.4c01005

Author Contributions

R.L. and E.L. conceived the study and designed experiments. R.L. performed most of the experiments and data analysis with additional help from B.J.L. R.L. and E.L. wrote the manuscript. R.L., B.J.L., and E.L. edited the manuscript.

Funding

R.L., B.J.L., and E.L. were supported by the National Institutes of Health (HL165135; CA279560) and the NSF Career Award (CBET #2338610).

Notes

The authors declare no competing financial interest.

ACKNOWLEDGMENTS

We thank Prof. Young-Kwon Hong (University of Southern California) for providing primary human lymphatic endothelial cells (LECs), Prof. Hai-Quan Mao, and Dr. Gregory Howard (Johns Hopkins University) for providing PLGA-*b*-PEG nanoparticles. We thank Issahy Cano and Anna M. Kolarzyk for their insightful discussion. This work was performed in part at the Cornell NanoScale Facility (CNF), a member of the National Nanotechnology Coordinated Infrastructure (NNCI), which is supported by the National Science Foundation (grant NNCI-2025233).

REFERENCES

(1) Hu, Z.; Zhao, X.; Wu, Z.; Qu, B.; Yuan, M.; Xing, Y.; Song, Y.; Wang, Z. Lymphatic vessel: origin, heterogeneity, biological functions, and therapeutic targets. *Signal Transduction Targeted Ther.* **2024**, *9* (1), 9. From NLM

(2) Lu, R.; Soden, P. A.; Lee, E. Tissue-Engineered Models for Glaucoma Research. *Micromachines (Basel)* **2020**, *11* (6), 612.

(3) Wu, A.; Lu, R.; Lee, E. Tissue engineering in age-related macular degeneration: a mini-review. *J. Biol. Eng.* **2022**, *16* (1), 11.

(4) Ilan, I. S.; Yslas, A. R.; Peng, Y.; Lu, R.; Lee, E. A 3D Human Lymphatic Vessel-on-Chip Reveals the Roles of Interstitial Flow and VEGF-A/C for Lymphatic Sprouting and Discontinuous Junction Formation. *Cell. Mol. Bioeng.* **2023**, *16* (4), 325−339.

(5) Alitalo, K. The lymphatic vasculature in disease. *Nat. Med.* **2011**, *17* (11), 1371−1380.

(6) Achen, M. G.; Stacker, S. A. Molecular control of lymphatic metastasis. *Ann. N.Y. Acad. Sci.* **2008**, *1131* (1), 225−234.

(7) Lee, J.; Kang, S.; Park, H.; Sun, J. G.; Kim, E. C.; Shim, G. Nanoparticles for Lymph Node-Directed Delivery. *Pharmaceutics* **2023**, *15* (2), 565.

(8) Li, Z.-Z.; Zhong, N.-N.; Cao, L.-M.; Cai, Z.-M.; Xiao, Y.; Wang, G.-R.; Liu, B.; Xu, C.; Bu, L.-L. Nanoparticles Targeting Lymph Nodes for Cancer Immunotherapy: Strategies and Influencing Factors. *Small* **2024**, *20* (19), No. e2308731.

(9) Sestito, L. F.; To, K. H.; Cribb, M. T.; Archer, P. A.; Thomas, S. N.; Dixon, J. B. Lymphatic-draining nanoparticles deliver Bay K8644 payload to lymphatic vessels and enhance their pumping function. *Sci. Adv.* **2023**, *9* (8), No. eabq0435.

(10) Wang, Y.; Wang, H. Lymph node targeting for immunotherapy. *Immuno-Oncol Technol.* **2023**, *20*, No. 100395.

(11) Qin, X.; Pan, L.; Chen, T.; Li, D.; Lin, X.; Li, G.; Feng, C.; Ye, W.; Liang, W.; Chen, J.; Wang, Q. Inflammation-responsive nanoparticles suppress lymphatic clearance for prolonged arthritis therapy. *J. Controlled Release* **2022**, *352*, 700−711.

(12) Bahmani, B.; Vohra, I.; Kamaly, N.; Abdi, R. Active targeted delivery of immune therapeutics to lymph nodes. *Curr. Opin. Organ Transplant.* **2018**, *23* (1), 8−14.

(13) O'Melia, M. J.; Thomas, S. N. Lymphatics drain nanoparticles from tumours. *Nat. Mater.* **2023**, *22* (11), 1287−1288.

(14) McCright, J.; Naiknavare, R.; Yarmovsky, J.; Maisel, K. Targeting Lymphatics for Nanoparticle Drug Delivery. *Front. Pharmacol.* **2022**, *13*, No. 887402.

(15) Randolph, G. J.; Angeli, V.; Swartz, M. A. Dendritic-cell trafficking to lymph nodes through lymphatic vessels. *Nat. Rev. Immunol.* **2005**, *5* (8), 617−628.

(16) Reddy, S. T.; van der Vlies, A. J.; Simeoni, E.; Angeli, V.; Randolph, G. J.; O'Neil, C. P.; Lee, L. K.; Swartz, M. A.; Hubbell, J. A. Exploiting lymphatic transport and complement activation in nanoparticle vaccines. *Nat. Biotechnol.* **2007**, *25* (10), 1159−1164.

(17) Howard, G. P.; Verma, G.; Ke, X.; Thayer, W. M.; Hamerly, T.; Baxter, V. K.; Lee, J. E.; Dinglasan, R. R.; Mao, H.-Q. Critical Size Limit of Biodegradable Nanoparticles for Enhanced Lymph Node Trafficking and Paracortex Penetration. *Nano Res.* **2019**, *12* (4), 837−844.

(18) Chen, J.; Ye, Z.; Huang, C.; Qiu, M.; Song, D.; Li, Y.; Xu, Q. Lipid nanoparticle-mediated lymph node-targeting delivery of mRNA cancer vaccine elicits robust CD8(+) T cell response. *Proc. Natl. Acad. Sci. U. S. A.* **2022**, *119* (34), No. e2207841119.

(19) Thomas, S. N.; Vokali, E.; Lund, A. W.; Hubbell, J. A.; Swartz, M. A. Targeting the tumor-draining lymph node with adjuvanted nanoparticles reshapes the anti-tumor immune response. *Biomaterials* **2014**, *35* (2), 814−824.

(20) Schudel, A.; Chapman, A. P.; Yau, M.-K.; Higginson, C. J.; Francis, D. M.; Manspeaker, M. P.; Avecilla, A. R. C.; Rohner, N. A.; Finn, M. G.; Thomas, S. N. Programmable multistage drug delivery to lymph nodes. *Nat. Nanotechnol.* **2020**, *15* (6), 491−499.

(21) Han, S.; Quach, T.; Hu, L.; Wahab, A.; Charman, W. N.; Stella, V. J.; Trevaskis, N. L.; Simpson, J. S.; Porter, C. J. H. Targeted delivery of a model immunomodulator to the lymphatic system: Comparison of alkyl ester versus triglyceride mimetic lipid prodrug strategies. *J. Controlled Release* **2014**, *177*, 1−10.

(22) He, P.; Tang, H.; Zheng, Y.; Xiong, Y.; Cheng, H.; Li, J.; Zhang, Y.; Liu, G. Advances in nanomedicines for lymphatic imaging and therapy. *J. Nanobiotechnol.* **2023**, *21* (1), 292.

(23) Metselaar, J. M.; Lammers, T. Challenges in nanomedicine clinical translation. *Drug Delivery Transl. Res.* **2020**, *10* (3), 721−725.

(24) Trevaskis, N. L.; Kaminskas, L. M.; Porter, C. J. From sewer to saviour—targeting the lymphatic system to promote drug exposure and activity. *Nat. Rev. Drug Discovery* **2015**, *14* (11), 781−803.

(25) Ho, D. N.; Kohler, N.; Sigdel, A.; Kalluri, R.; Morgan, J. R.; Xu, C.; Sun, S. Penetration of endothelial cell coated multicellular tumor

spheroids by iron oxide nanoparticles. *Theranostics* **2012**, *2* (1), 66−75.
(26) Kim, B.; Han, G.; Toley, B. J.; Kim, C.-k.; Rotello, V. M.; Forbes, N. S. Tuning payload delivery in tumour cylindroids using gold nanoparticles. *Nat. Nanotechnol.* **2010**, *5* (6), 465−472.
(27) Hou, X.; Liu, S.; Wang, M.; Wiraja, C.; Huang, W.; Chan, P.; Tan, T.; Xu, C. Layer-by-Layer 3D Constructs of Fibroblasts in Hydrogel for Examining Transdermal Penetration Capability of Nanoparticles. *SLAS Technol.* **2017**, *22* (4), 447−453.
(28) Sun, M.; Lee, J.; Chen, Y.; Hoshino, K. Studies of nanoparticle delivery with in vitro bio-engineered microtissues. *Bioact. Mater.* **2020**, *5* (4), 924−937.
(29) McCright, J.; Yarmovsky, J.; Maisel, K. Para- and Transcellular Transport Kinetics of Nanoparticles across Lymphatic Endothelial Cells. *Mol. Pharmaceutics* **2024**, *21* (3), 1160−1169.
(30) Åberg, C. Quantitative analysis of nanoparticle transport through in vitro blood-brain barrier models. *Tissue Barriers* **2016**, *4* (1), No. e1143545.
(31) Strugari, A. F. G.; Stan, M. S.; Gharbia, S.; Hermenean, A.; Dinischiotu, A. Characterization of Nanoparticle Intestinal Transport Using an In Vitro Co-Culture Model. *Nanomaterials* **2018**, *9* (1), 5.
(32) Kraus, S.; Lee, E. A human initial lymphatic chip reveals distinct mechanisms of primary lymphatic valve dysfunction in acute and chronic inflammation. *Lab Chip* **2023**, *23* (24), 5180−5194. From NLM
(33) Soden, P. A.; Henderson, A. R.; Lee, E. A Microfluidic Model of AQP4 Polarization Dynamics and Fluid Transport in the Healthy and Inflamed Human Brain: The First Step Towards Glymphatics-on-a-Chip. *Adv. Biol.* **2022**, *6* (12), No. e2200027.
(34) Nguyen, D. T.; Lee, E.; Alimperti, S.; Norgard, R. J.; Wong, A.; Lee, J. J.; Eyckmans, J.; Stanger, B. Z.; Chen, C. S. A biomimetic pancreatic cancer on-chip reveals endothelial ablation via ALK7 signaling. *Sci. Adv.* **2019**, *5* (8), No. eaav6789.
(35) Wang, H.-F.; Ran, R.; Liu, Y.; Hui, Y.; Zeng, B.; Chen, D.; Weitz, D. A.; Zhao, C.-X. Tumor-Vasculature-on-a-Chip for Investigating Nanoparticle Extravasation and Tumor Accumulation. *ACS Nano* **2018**, *12* (11), 11600−11609.
(36) Lee, E.; Chan, S. L.; Lee, Y.; Polacheck, W. J.; Kwak, S.; Wen, A.; Nguyen, D. T.; Kutys, M. L.; Alimperti, S.; Kolarzyk, A. M.; et al. A 3D biomimetic model of lymphatics reveals cell-cell junction tightening and lymphedema via a cytokine-induced ROCK2/JAM-A complex. *Proc. Natl. Acad. Sci. U. S. A.* **2023**, *120* (41), No. e2308941120.
(37) Choi, D.; Park, E.; Jung, E.; Seong, Y. J.; Yoo, J.; Lee, E.; Hong, M.; Lee, S.; Ishida, H.; Burford, J.; et al. Laminar flow downregulates Notch activity to promote lymphatic sprouting. *J. Clin Invest* **2017**, *127* (4), 1225−1240.
(38) Choi, D.; Park, E.; Choi, J.; Lu, R.; Yu, J. S.; Kim, C.; Zhao, L.; Yu, J.; Nakashima, B.; Lee, S.; et al. Piezo1 regulates meningeal lymphatic vessel drainage and alleviates excessive CSF accumulation. *Nat. Neurosci.* **2024**, *27* (5), 913−926.
(39) Polacheck, W. J.; Kutys, M. L.; Tefft, J. B.; Chen, C. S. Microfabricated blood vessels for modeling the vascular transport barrier. *Nat. Protoc.* **2019**, *14* (5), 1425−1454. From NLM
(40) Kwak, T. J.; Lee, E. Rapid multilayer microfabrication for modeling organotropic metastasis in breast cancer. *Biofabrication* **2020**, *13* (1), No. 015002.
(41) Schulte-Merker, S.; Sabine, A.; Petrova, T. V. Lymphatic vascular morphogenesis in development, physiology, and disease. *J. Cell Biol.* **2011**, *193* (4), 607−618. From NLM
(42) Polacheck, W. J.; Kutys, M. L.; Yang, J.; Eyckmans, J.; Wu, Y.; Vasavada, H.; Hirschi, K. K.; Chen, C. S. A non-canonical Notch complex regulates adherens junctions and vascular barrier function. *Nature* **2017**, *552* (7684), 258−262. From NLM
(43) van Duinen, V.; van den Heuvel, A.; Trietsch, S. J.; Lanz, H. L.; van Gils, J. M.; van Zonneveld, A. J.; Vulto, P.; Hankemeier, T. 96 perfusable blood vessels to study vascular permeability in vitro. *Sci. Rep.* **2017**, *7* (1), 18071. From NLM
(44) Schneider, C. A.; Rasband, W. S.; Eliceiri, K. W. NIH Image to ImageJ: 25 years of image analysis. *Nat. Methods* **2012**, *9* (7), 671−675.
(45) Thévenaz, P.; Ruttimann, U. E.; Unser, M. A pyramid approach to subpixel registration based on intensity. *IEEE Trans. Image Process.* **1998**, *7* (1), 27−41. From NLM
(46) Bolte, S.; Cordelières, F. P. A guided tour into subcellular colocalization analysis in light microscopy. *J. Microsc.* **2006**, *224* (3), 213−232.
(47) Yang, Y. L.; Motte, S.; Kaufman, L. J. Pore size variable type I collagen gels and their interaction with glioma cells. *Biomaterials* **2010**, *31* (21), 5678−5688. From NLM
(48) Haq, F.; Ahmed, N.; Qasim, M. Comparative genomic analysis of collagen gene diversity. *3 Biotech* **2019**, *9* (3), 83. From NLM
(49) Mohammad, A. K.; Reineke, J. J. Quantitative detection of PLGA nanoparticle degradation in tissues following intravenous administration. *Mol. Pharmaceutics* **2013**, *10* (6), 2183−2189. From NLM
(50) Rescignano, N.; Tarpani, L.; Romani, A.; Bicchi, I.; Mattioli, S.; Emiliani, C.; Torre, L.; Kenny, J. M.; Martino, S.; Latterini, L.; Armentano, I. In-vitro degradation of PLGA nanoparticles in aqueous medium and in stem cell cultures by monitoring the cargo fluorescence spectrum. *Polym. Degrad. Stab.* **2016**, *134*, 296−304.
(51) Fick, A. On liquid diffusion. *J. Membr. Sci.* **1995**, *100* (1), 33−38.
(52) McCright, J.; Skeen, C.; Yarmovsky, J.; Maisel, K.Dense poly(ethylene glycol) coatings maximize nanoparticle transport across lymphatic endothelial cells and accumulate in the skindraining lymph nodes. *bioRxiv* **2020**, DOI: . 2008. 2001.232249.
(53) Norden, P. R.; Kume, T. Molecular Mechanisms Controlling Lymphatic Endothelial Junction Integrity. *Front. Cell Dev. Biol.* **2020**, *8*, No. 627647.
(54) Triacca, V.; Güç, E.; Kilarski, W. W.; Pisano, M.; Swartz, M. A. Transcellular Pathways in Lymphatic Endothelial Cells Regulate Changes in Solute Transport by Fluid Stress. *Circ. Res.* **2017**, *120* (9), 1440−1452.
(55) Predescu, D.; Vogel, S. M.; Malik, A. B. Functional and morphological studies of protein transcytosis in continuous endothelia. *Am. J. Physiol.: Lung Cell. Mol. Physiol.* **2004**, *287* (5), L895−901.
(56) Rennick, J. J.; Johnston, A. P. R.; Parton, R. G. Key principles and methods for studying the endocytosis of biological and nanoparticle therapeutics. *Nat. Nanotechnol.* **2021**, *16* (3), 266−276. From NLM
(57) Bucci, C.; Thomsen, P.; Nicoziani, P.; McCarthy, J.; van Deurs, B. Rab7: a key to lysosome biogenesis. *Mol. Biol. Cell* **2000**, *11* (2), 467−480.
(58) Candela, P.; Gosselet, F.; Miller, F.; Buee-Scherrer, V.; Torpier, G.; Cecchelli, R.; Fenart, L. Physiological pathway for low-density lipoproteins across the blood-brain barrier: transcytosis through brain capillary endothelial cells in vitro. *Endothelium* **2008**, *15* (5−6), 254−264. From NLM
(59) Reddy, S. T.; Rehor, A.; Schmoekel, H. G.; Hubbell, J. A.; Swartz, M. A. In vivo targeting of dendritic cells in lymph nodes with poly(propylene sulfide) nanoparticles. *J. Controlled Release* **2006**, *112* (1), 26−34.
(60) Rohner, N. A.; Thomas, S. N. Flexible Macromolecule versus Rigid Particle Retention in the Injected Skin and Accumulation in Draining Lymph Nodes Are Differentially Influenced by Hydrodynamic Size. *ACS Biomater. Sci. Eng.* **2017**, *3* (2), 153−159.
(61) Kulkarni, S. A.; Feng, S. S. Effects of particle size and surface modification on cellular uptake and biodistribution of polymeric nanoparticles for drug delivery. *Pharm. Res.* **2013**, *30* (10), 2512−2522. From NLM
(62) Zhang, Y.-N.; Lazarovits, J.; Poon, W.; Ouyang, B.; Nguyen, L. N. M.; Kingston, B. R.; Chan, W. C. W. Nanoparticle Size Influences Antigen Retention and Presentation in Lymph Node Follicles for Humoral Immunity. *Nano Lett.* **2019**, *19* (10), 7226−7235. From NLM

https://doi.org/10.1021/acsbiomaterials.4c01005
ACS Biomater. Sci. Eng. XXXX, XXX, XXX−XXX

(63) Lieleg, O.; Baumgärtel, R. M.; Bausch, A. R. Selective filtering of particles by the extracellular matrix: an electrostatic bandpass. *Biophys. J.* **2009**, *97* (6), 1569−1577.
(64) Perrault, S. D.; Walkey, C.; Jennings, T.; Fischer, H. C.; Chan, W. C. Mediating tumor targeting efficiency of nanoparticles through design. *Nano Lett.* **2009**, *9* (5), 1909−1915.
(65) He, X.; Yang, Y.; Han, Y.; Cao, C.; Zhang, Z.; Li, L.; Xiao, C.; Guo, H.; Wang, L.; Han, L.; et al. Extracellular matrix physical properties govern the diffusion of nanoparticles in tumor microenvironment. *Proc. Natl. Acad. Sci. U. S. A.* **2023**, *120* (1), No. e2209260120.
(66) Mair, L.; Superfine, R. Single particle tracking reveals biphasic transport during nanorod magnetophoresis through extracellular matrix. *Soft Matter* **2014**, *10* (23), 4118−4125.
(67) Engin, A. B.; Nikitovic, D.; Neagu, M.; Henrich-Noack, P.; Docea, A. O.; Shtilman, M. I.; Golokhvast, K.; Tsatsakis, A. M. Mechanistic understanding of nanoparticles' interactions with extracellular matrix: the cell and immune system. *Part. Fibre Toxicol.* **2017**, *14* (1), 22.
(68) Karamanos, N. K.; Theocharis, A. D.; Piperigkou, Z.; Manou, D.; Passi, A.; Skandalis, S. S.; Vynios, D. H.; Orian-Rousseau, V.; Ricard-Blum, S.; Schmelzer, C. E. H.; et al. A guide to the composition and functions of the extracellular matrix. *FEBS J.* **2021**, *288* (24), 6850−6912.
(69) Roig-Rosello, E.; Rousselle, P. The Human Epidermal Basement Membrane: A Shaped and Cell Instructive Platform That Aging Slowly Alters. *Biomolecules* **2020**, *10* (12), 1607. From NLM
(70) Li, S.-D.; Huang, L. Pharmacokinetics and biodistribution of nanoparticles. *Mol. Pharmaceutics* **2008**, *5* (4), 496−504.
(71) Barua, S.; Mitragotri, S. Challenges associated with Penetration of Nanoparticles across Cell and Tissue Barriers: A Review of Current Status and Future Prospects. *Nano Today* **2014**, *9* (2), 223−243.
(72) Ye, D.; Raghnaill, M. N.; Bramini, M.; Mahon, E.; Åberg, C.; Salvati, A.; Dawson, K. A. Nanoparticle accumulation and transcytosis in brain endothelial cell layers. *Nanoscale* **2013**, *5* (22), 11153−11165.
(73) Khan, A. I.; Lu, Q.; Du, D.; Lin, Y.; Dutta, P. Quantification of kinetic rate constants for transcytosis of polymeric nanoparticle through blood-brain barrier. *Biochim. Biophys. Acta, Gen. Subj.* **2018**, *1862* (12), 2779−2787.
(74) Cong, V. T.; Tilley, R. D.; Sharbeen, G.; Phillips, P. A.; Gaus, K.; Gooding, J. J. How to exploit different endocytosis pathways to allow selective delivery of anticancer drugs to cancer cells over healthy cells. *Chem. Sci.* **2021**, *12* (46), 15407−15417. From NLM
(75) Niaz, S.; Forbes, B.; Raimi-Abraham, B. T. Exploiting Endocytosis for Non-Spherical Nanoparticle Cellular Uptake. *Nanomanufacturing* **2022**, *2* (1), 1−16.

https://doi.org/10.1021/acsbiomaterials.4c01005
ACS Biomater. Sci. Eng. XXXX, XXX, XXX−XXX